

# Automated identification of neurons and their locations

A. INGLIS\*, L. CRUZ\*, D. L. ROE†, H. E. STANLEY\*,  
D. L. ROSENE†‡ & B. URBANC\*

\*Center for Polymer Studies, Department of Physics, Boston University, Boston, MA 02215, U.S.A.

†Department of Anatomy and Neurobiology, Boston University School of Medicine, Boston, MA 02118, U.S.A.

‡Yerkes National Primate Research Center, Emory University, Atlanta, GA 30322, U.S.A.

**Key words.** Active contours, artificial neural network, neuron identification, Nissl-stain, training.

## Summary

Individual locations of many neuronal cell bodies ( $>10^4$ ) are needed to enable statistically significant measurements of spatial organization within the brain such as nearest-neighbour and microcolumnarity measurements. In this paper, we introduce an Automated Neuron Recognition Algorithm (ANRA) which obtains the  $(x, y)$  location of individual neurons within digitized images of Nissl-stained, 30  $\mu\text{m}$  thick, frozen sections of the cerebral cortex of the Rhesus monkey. Identification of neurons within such Nissl-stained sections is inherently difficult due to the variability in neuron staining, the overlap of neurons, the presence of partial or damaged neurons at tissue surfaces, and the presence of non-neuron objects, such as glial cells, blood vessels, and random artefacts. To overcome these challenges and identify neurons, ANRA applies a combination of image segmentation and machine learning. The steps involve active contour segmentation to find outlines of potential neuron cell bodies followed by artificial neural network training using the segmentation properties (size, optical density, gyration, etc.) to distinguish between neuron and non-neuron segmentations. ANRA positively identifies  $86 \pm 5\%$  neurons with  $15 \pm 8\%$  error (mean  $\pm$  SD) on a wide range of Nissl-stained images, whereas semi-automatic methods obtain  $80 \pm 7\%/17 \pm 12\%$ . A further advantage of ANRA is that it affords an unlimited increase in speed from semi-automatic methods, and is computationally efficient, with the ability to recognize  $\sim 100$  neurons per minute using a standard personal computer. ANRA is amenable to analysis of huge photo-montages of Nissl-stained tissue, thereby opening the door to fast, efficient and quantitative analysis of vast stores of archival material that exist in laboratories and research collections around the world.

Correspondence to: A. Inglis. Tel: 617 353 8000; fax: 617 353 9393; e-mail: ainglis@physics.bu.edu

## Introduction

Since the 1980s, the application of unbiased stereological approaches to quantify objects of biological interest has allowed for rigorous measurements of many parameters of brain structure including total neuron number, area, and volume. These approaches are based on systematic random sampling from defined regions of interest using unbiased estimators (Mayhew, 1991; Schmitz & Hof, 2005). Although these measurements have produced extremely valuable insights into the structural organization of the brain, including age-related preservation of neuron numbers (Peters *et al.*, 1998), these 'first order' stereological parameters only partially describe the structural organization of the brain, as they cannot efficiently quantify 'second order' parameters that measure more complex spatial properties of neuron organization, such as the nearest neighbour arrangement (Asare, 1996; Duyckaerts & Godefroy, 2000; Schmitz *et al.*, 2002; Urbanc *et al.*, 2002; Hof *et al.*, 2003; Krasnoperov & Stoyan, 2004) and arrangement into mini- or microcolumns (Buxhoeveden & Lefkowitz, 1996; Buldyrev *et al.*, 2000; Cruz *et al.*, 2005).

Several approaches can be used to quantify 'second order' parameters. Stereological methods can quantify nearest-neighbour arrangement (Schmitz *et al.*, 2002), but the methods are labour intensive and would be difficult to apply to large brain areas. Image Fourier methods do not require manual marking of neuron locations and can quantify 'vertical bias' of objects within an image (Casanova *et al.*, 2006), but do not discern between the contribution from glial and neuronal cell bodies.

Alternatively, pair correlation methods use concepts from statistical physics to calculate correlation properties such as cross-correlation between two different types of objects (Urbanc *et al.*, 2002) and microcolumnar organization (Buldyrev *et al.*, 2000) of neurons, as well as more discerning

properties of spatial arrangement, such as the strength of microcolumnar order and microcolumnar width and length (Cruz *et al.*, 2005). The multitude of spatial organization quantities that can be calculated with pair correlation analysis makes it appealing to apply to large brain areas. To do that, we first need to address the major challenge to this approach: how to obtain the necessarily large number of neuron locations ( $10^3$ – $10^4$  locations per measurement) to get statistically significant results (see Section 'Density map method and microcolumnar strength' and 'Discussion') over large regions of the brain, reaching  $\sim 10^6$  for a large study. The acquisition of such numbers of neurons by manually or semi-automatically identifying and marking the location of each is prohibitively time-consuming and open to user bias. Hence, correlative analysis of spatial relationships among neurons [as well as non-stereology based cell counts (Todtenkopf *et al.*, 2005)] would be dramatically facilitated by an automatic method for identifying and locating the visible centres of neurons accurately and efficiently.

Although various other immunohistochemical methods could facilitate automated discrimination of neurons and glia better than Nissl, there are important advantages to develop automated methods for Nissl-stained tissue. Nissl-staining is the least expensive, easiest applied method for staining both neurons and glia. Furthermore, there are thousands of unique and often irreproducible collections of Nissl-stained brain material in clinical and research labs around the world that could be analyzed using the Automated Neuron Recognition Algorithm (ANRA).

There are several challenges to automatically retrieve neuron locations from two-dimensional digitized images of Nissl-stained brain tissue (Fig. 2a). A major challenge is to distinguish between neuron and non-neuron objects, including staining errors, tissue folds, and dirt particles, as well as blood vessels and glial cells. Another challenge is to identify neurons that differ almost as widely from each other as they do from non-neuronal objects. Neuron cell bodies are naturally diverse in size and shape and have different orientations with respect to their dendrite and axon processes. Neurons can also be cleaved at the cutting surface or damaged by the cutting process, which affects their shape in the tissue. These variables lead to diverse neuron cell profiles within the tissue slice. A further challenge is to discriminate between neurons that overlap, a common finding as tissue sections are 3D volumes projected onto a 2D image.

There are currently several published approaches to automatic retrieval of cell bodies from images. Some methods use segmentation techniques based on thresholding (Slater *et al.*, 1996; Benali *et al.*, 2003), Potts model (Peng *et al.*, 2003), watershed (Lin *et al.*, 2005), and active contours (Ray *et al.*, 2002). Others use trained neural networks to mark appropriately sized 'pixel patches' as cells of interest. The 'pixel patch' training methods use artificial neural networks (Sjöström *et al.*, 1999), local linear mapping (Nattkemper *et al.*,

2001), Fischer's linear discriminant (Long *et al.*, 2005) and support vector machines (Long *et al.*, 2006). Another method based on template matching has been recently introduced by Costa & Bollt (2006).

In this paper, we introduce and test an ANRA (Fig. 1) which uses a combination of segmenting and training to overcome the challenges of retrieving neuron location in Nissl-stained tissue sections. ANRA automatically identifies neurons from digital images and retrieves their ( $x, y$ ) locations.

## Methods

### *Image input and preprocessing*

The inputs for ANRA are photomicrographs of 30  $\mu\text{m}$  thick Nissl-stained tissue sections taken at  $10\times$  magnification and a resolution of 1.5  $\mu\text{m}$  per pixel. Because the 30  $\mu\text{m}$  tissue section shrinks during processing to a thickness of less than 10  $\mu\text{m}$ , all of the tissue is in focus when viewed at microscopic magnifications of  $20\times$  or lower, thus the 2D image properly represents neuron locations. Since the colour information is not as useful in the monotone Nissl-stained images (Fig. 2a) the images are converted to grey scale images ranging from 0 (black) to 255 (white).

The photomicrographs are taken from different areas of the brain from different subjects at different times. Therefore, images are of different 'quality', reflecting a combination of variations in morphology, staining, slide preparation, and digitization (Fig. 2b). To reduce this variability, the images are first 'normalized' such that every image has the same background and foreground average optical density. This is done by thresholding each image into foreground and background pixels and finding the average optical density for the foreground and background separately. For each image, the optical density histogram is then shifted to match the foreground/background averages of an ideal image (Fig. 3a). Figure 3(b) shows the images final normalization as compared to the original images in Fig. 2(b). This preprocessing step removes most of the image variations due to processing (staining, slide preparation, digitization, etc.) and is a key step toward applying ANRA to an unlimited number of images that do not vary drastically in intrinsic morphological differences (neuron density, shape, size, etc.). There is no need for other preprocessing steps such as blurring or sharpening since ANRA, by design, overcomes the challenges of noisy images and weak boundary information.

### *Main segmentation tool: OSM*

Here we describe the segmentation procedure presented in Fig. 1, called the overall segmentation method (OSM).

*Overmarking the image.* An initial step of the segmentation process is 'seeding' the image with one or more points for each possible neuron cell body. A combination of two methods is

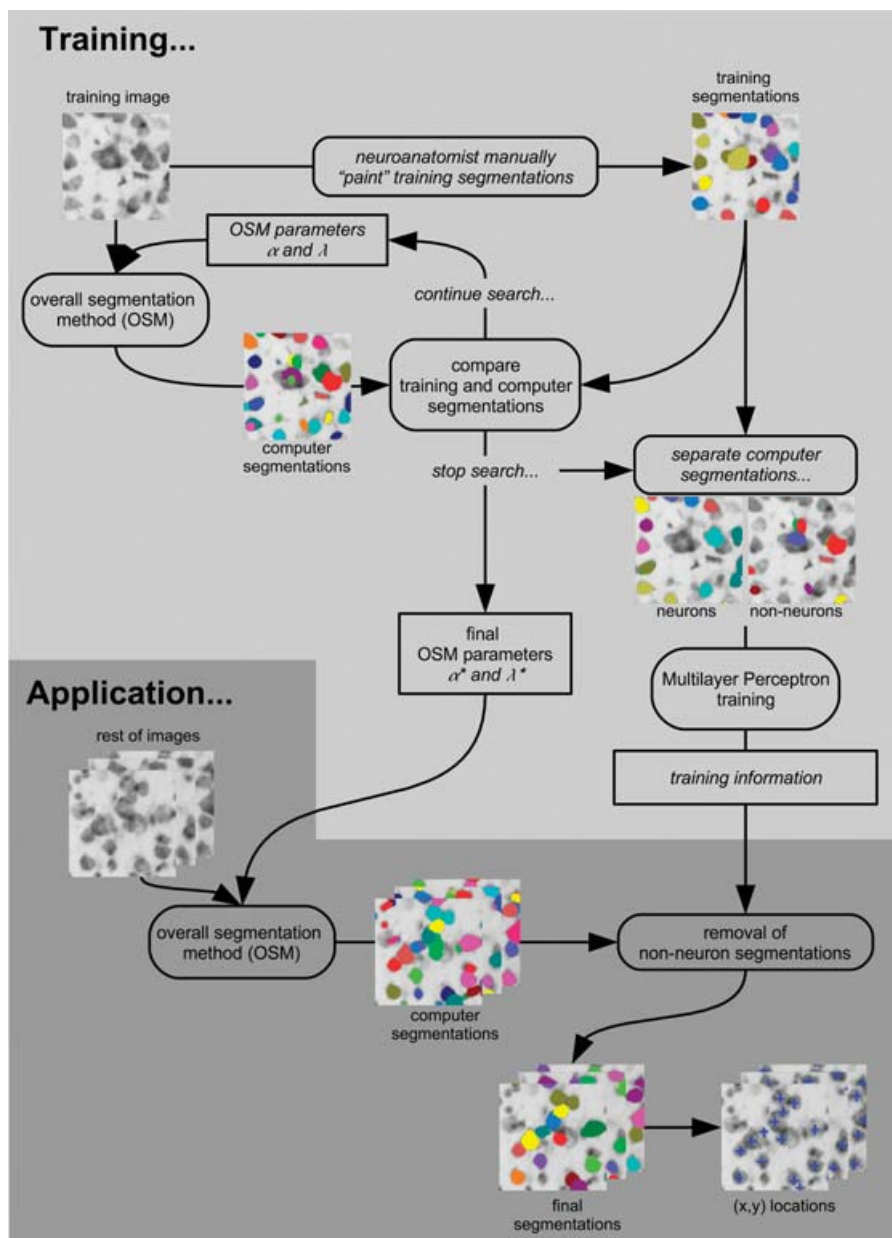


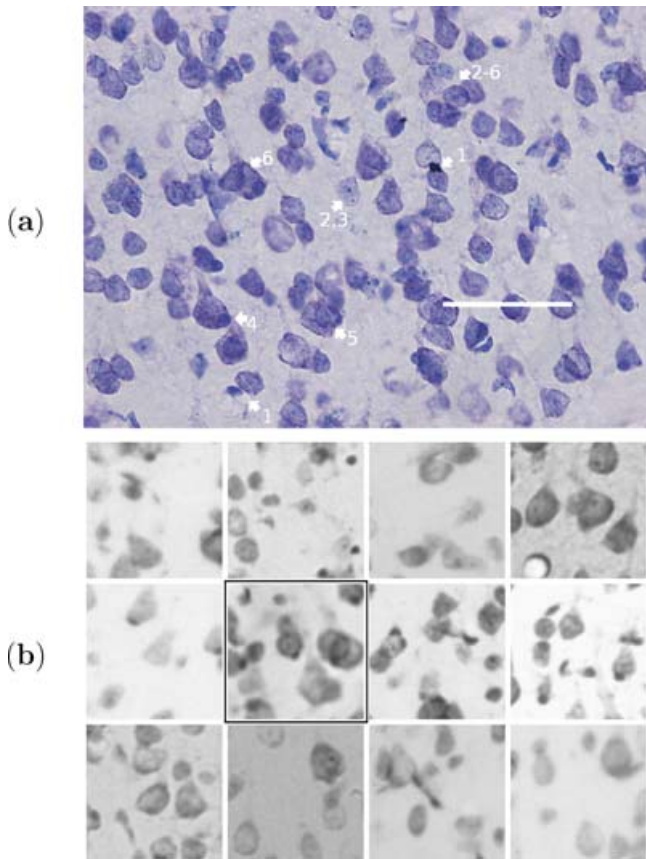
**Fig. 1.** A schematic diagram showing processes involved in the Automated Neuron Recognition Algorithm (ANRA). The schematic describes the two main steps of the algorithm: training and application. Rectangles denote parameters that pass through the algorithm. Ovals, such as the OSM, are the computational parts of the algorithm, which can have images, segmentations, and parameters as their inputs and outputs.

used (Fig. 4a): a hexagonal grid of points is placed over the thresholded foreground of the image and the centre points of objects identified by the traditional watershed segmentation (Javi, 2002).

*Active contour segmentation.* We employ active contour segmentation with statistical shape knowledge (Cremers *et al.*, 2000) because the method is designed to overcome the challenges of noisy images and missing boundary data, the main identification challenge in Nissl-stained tissue. Also,

the method uses low-dimensional shape representations which are ideal for modeling cell contours (outlines of cells). Because the image is initially overmarked, the calculations of contour splitting (Zimmer *et al.*, 2002) are not needed.

The image  $f_{ij}$  is a digital image of sliced brain tissue which defines the optical density (grey scale value) of each pixel ( $ij$ ). We assume that the image contains at least one type of object of interest (neurons) mixed with other objects (non-neurons). The goal of a single run of the segmentation is to 'segment' a single object of interest (a single neuron) from the rest of the



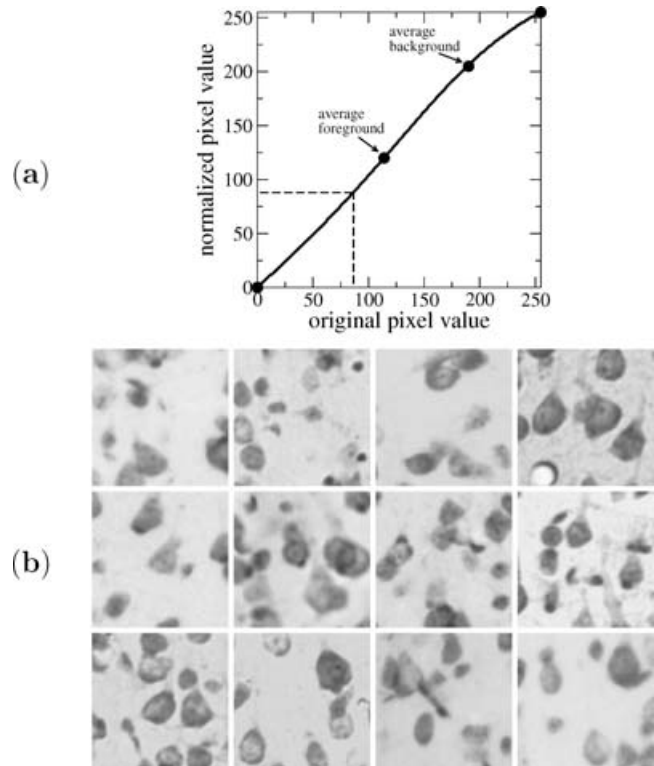
**Fig. 2.** Challenges of automated neuron recognition. (a) 20 $\times$  micrograph (scale bar: 50  $\mu$ m) of a typical section showing the difficulties of separating neurons from glial cells and other artefacts in Nissl-stained tissue: 1. capillaries, and unidentified material, 2. large glia (astrocytes), 3. glial as light as neurons in some cases, 4. neurons overlapped by glia (oligodendrocytes), 5. neurons overlapped by other neurons, 6. multiple neurons and glial overlapped. (b) 10 $\times$  micrograph examples showing varying image quality. The highlighted micrograph is selected as an 'ideal' contrast to be used in image normalization.

image (all other neurons, non-neurons, and background). It does this by 'evolving' a loop of pixels called a *contour* ( $C$ ) from a circle of typical neuron diameter (12  $\mu$ m) starting at one of the overmarked starting points, to a location and shape that surrounds a potential neuron cell body (Fig. 4b). This process is repeated for each starting location until all starting locations have been exhausted.

The movement of  $C$  is controlled by a set of  $N$  points called *control points*  $\{(x_n, y_n)\}_{n=1..N}$  for which we use the compact notation (Cremers *et al.*, 2000)

$$z = (\mathbf{r}_1, \dots, \mathbf{r}_N) = (x_1, y_1, \dots, x_N, y_N). \quad (1)$$

The control points are parameters in a closed quadratic Bezier-spline (B-spline) curve (Blake & Isard, 1998) that define the exact location (pixels) of  $C$  (see Fig. 5 for definition). Hence,  $C$  moves and changes shape by the iterative motion of the control points  $z$ . At each time step, each control point  $z$  makes a small



**Fig. 3.** (a) Preprocessing 'normalizes' the images so that they every image has the same background and foreground average optical densities, thereby removing the challenge of varying image type within Nissl-stained tissue. This is done by mapping optical density values of non-ideal images to an ideal image so that the average foreground and background averages are the same. The graph shows the optical density ranges of the ideal and non-ideal images (0..255), and a Bezier curve that passes through 4 points: (0,0), the background and foreground averages of the ideal and non-ideal images, and (255,255). (b) Examples of image normalization.

movement towards encircling an object close to its starting location by minimizing a total energy  $E$  based on two energy considerations,  $E_{MS}$  and  $E_c$ :

$$E(f, u, C) = E_{MS}(f, u) + \alpha E_c(C). \quad (2)$$

A qualitative understanding of the energy terms is presented in Fig. 6.  $E_{MS}$  is the Mumford–Shah energy term, which determines how well the contour separates lighter and darker grey scale regions in the image  $f_{ij}$ .  $E_c(C)$  is the contour energy term, which quantifies the similarity of the contour to a previously chosen set of training shapes (in our case, the training shapes are oval-like).  $E_{MS}$  is high when  $C$  does not separate different contrasts well, and is low if it does.  $E_c(C)$  is high if the shape is very contorted, and low if it is oval-like.  $\alpha$  changes the relative influence of the two energy terms. If  $\alpha$  is a high value, then  $C$  will evolve into a rigid perfect oval, ignoring all image information. If  $\alpha$  is zero, then  $C$  will surround any nearby object in the image with no regard to the final shape of  $C$ . When the two energy terms are balanced with an appropriate

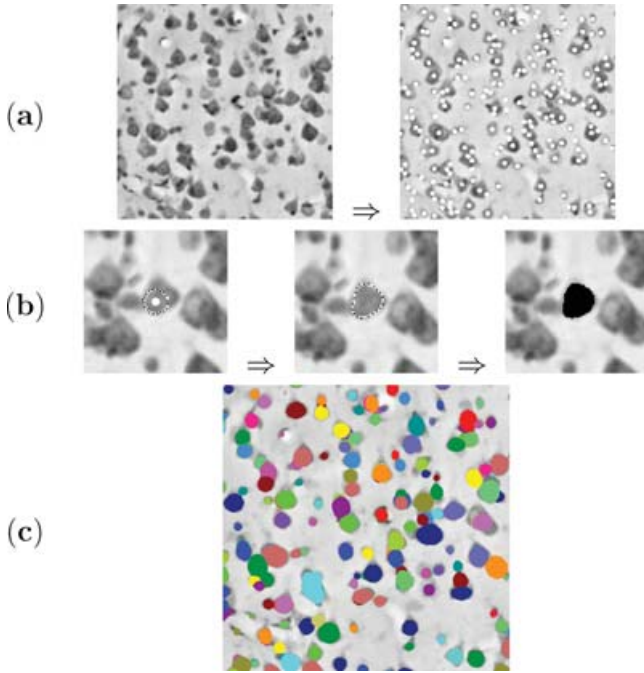


**Fig. 4.** Steps of the overall segmentation method (OSM). (a) Overmarking the image with a hexagonal grid of points that lay on the thresholded foreground and centre points of a traditional watershed segmentation. Points within 5 pixels are combined to avoid redundancy. (b) Active contour segmentation: using each starting location found in (a), a segmentation (clustering) process is performed within a small region of the image to find one possible neuron cell body. This process is then repeated for each starting location until all starting locations are exhausted. (c) The final set of *computer segments*, shown in different solid colours, is the output of the OSM.

$\alpha$  and the system is evolved to minimize  $E$  then objects in an image are encircled properly. Figure 7 shows a typical evolution of  $C$  with an appropriate  $\alpha$  value.  $u_{ij}$  is a variable image, similar to a blurred version of  $f_{ij}$ , which is used in the algorithm, as described below.

The *Mumford–Shah energy term*  $E_{MS}(f, u)$  quantifies the alignment of the contour with edges in the image  $f_{ij}$ :

$$E_{MS}(f, u) = \frac{1}{2} \sum_{ij} \{ [f_{ij} - u_{ij}(t)]^2 + \lambda^2 |\nabla u_{ij}(t)|^2 \}, \quad (3)$$

where  $\lambda$  is the Mumford–Shah energy parameter that determines relative strengths of the terms.  $|\nabla u_{ij}(t)|^2$  is the square of the magnitude of the picture gradient:

$$\begin{aligned} |\nabla u_{ij}(t)|^2 &= \left( \frac{\partial u}{\partial x} \right)^2 + \left( \frac{\partial u}{\partial y} \right)^2 \\ &= \frac{[u_{i+1,j}(t) - u_{i-1,j}(t)]^2 + [u_{i,j+1}(t) - u_{i,j-1}(t)]^2}{4}. \end{aligned} \quad (4)$$

It should be noted that Cremers *et al.* (2000) includes an additional term  $v\|C\|$  to Eq. (3), which minimizes the length  $\|C\|$  of the contour within its evolution. We do not include

this term because it adds an additional free parameter and does not contribute to the functionality of the algorithm when identifying cell shaped objects.

Equation (3) is differentiated with respect to control point movement. Setting the solution of the differentiation to a minimum of  $E_{MS}[f, u(t)]$  gives the evolution equation for each individual control point  $n = 1, \dots, N$  during each iteration  $dt$  (Mumford & Shah, 1989):

$$\begin{aligned} \dot{x}_n(t) &= (e^+ - e^-) \mathbf{n}_x \\ \dot{y}_n(t) &= (e^+ - e^-) \mathbf{n}_y, \end{aligned} \quad (5)$$

where  $e^+$  and  $e^-$  are  $E_{MS}$  (Eq. 3) summed over the single line of pixels right outside ( $e^+$ ) and right inside ( $e^-$ ) the segment of  $C$  centred around control point  $(x_n, y_n)$  (Fig. 8).  $\mathbf{n}_x$  and  $\mathbf{n}_y$  are the outer normal vectors of  $C$  at each control point  $\mathbf{r}_n$  in the  $x$  and  $y$  direction respectively.  $\dot{x} = dx/dt$  and  $\dot{y} = dy/dt$ , where  $t$  is the artificial time parameter.

Equation (3) is then differentiated with respect to the variable image  $u_{ij}$ . Setting the solution to a minimum of  $E_{MS}[f, u(t)]$  gives the evolution equation for each pixel  $u_{ij}$  during each iteration  $dt$  (Mumford & Shah, 1989):

$$\begin{aligned} u_{ij}(t + dt) &= \begin{cases} u_{ij}(t) + \{ f_{ij} - u_{ij}(t) + \lambda^2 \nabla^2 u_{ij}(t) \} dt & \text{if } ij \in C \\ u_{ij}(t) & \text{if } ij \in C^c. \end{cases} \end{aligned} \quad (6)$$

At  $t = 0$ ,  $u_{ij}(0) = f_{ij}$ .  $\nabla^2 u_{ij}(t)$  is the Laplacian in 2D Cartesian coordinates:

$$\begin{aligned} \nabla^2 u_{ij}(t) &= \left( \frac{\partial^2 u}{\partial x^2} \right) + \left( \frac{\partial^2 u}{\partial y^2} \right) \\ &= u_{i+1,j} + u_{i-1,j} + u_{i,j+1} + u_{i,j-1} - 4u_{i,j} \end{aligned} \quad (7)$$

Equation (6) describes a diffusion  $[\nabla^2 u_{ij}(t)]$  process limited by the original image  $[f_{ij} - u_{ij}(t)]$ . The key component is that  $u_{ij}$  never evolves at the pixels that make up  $C$ .  $u_{ij}$  becomes stable once  $C$  separates contrasted regions. Therefore, minimizing  $E_{MS}$  tends to evolve  $C$  so that the grey scale values vary slowly (smoothly) in the areas inside and outside the contour but vary strongly (discontinuously) across the contour  $C$ .

The *contour energy term*  $E_c$  affects the shape of the contour irrespective of the images  $f_{ij}$  and  $u_{ij}$ .  $E_c$  is minimized for contour shapes most similar to a previously chosen set of training shapes  $\chi = \{z_1, z_2, \dots\}$ . The energy is calculated using the following equation:

$$E_c(C) = \frac{1}{2} (z - z_0)^T \Sigma^{-1} (z - z_0), \quad (8)$$

where the vector  $z_0$  and the matrix  $\Sigma$  (with an inverse  $\Sigma^{-1}$ ) contain the mean and covariant information of the previously chosen set of training shapes  $\chi = \{z_1, z_2, \dots\}$ :

$$z_0 = \langle z_i \rangle \quad (9)$$

$$\Sigma = \langle (z_i - z_0)^T (z_i - z_0) \rangle. \quad (10)$$

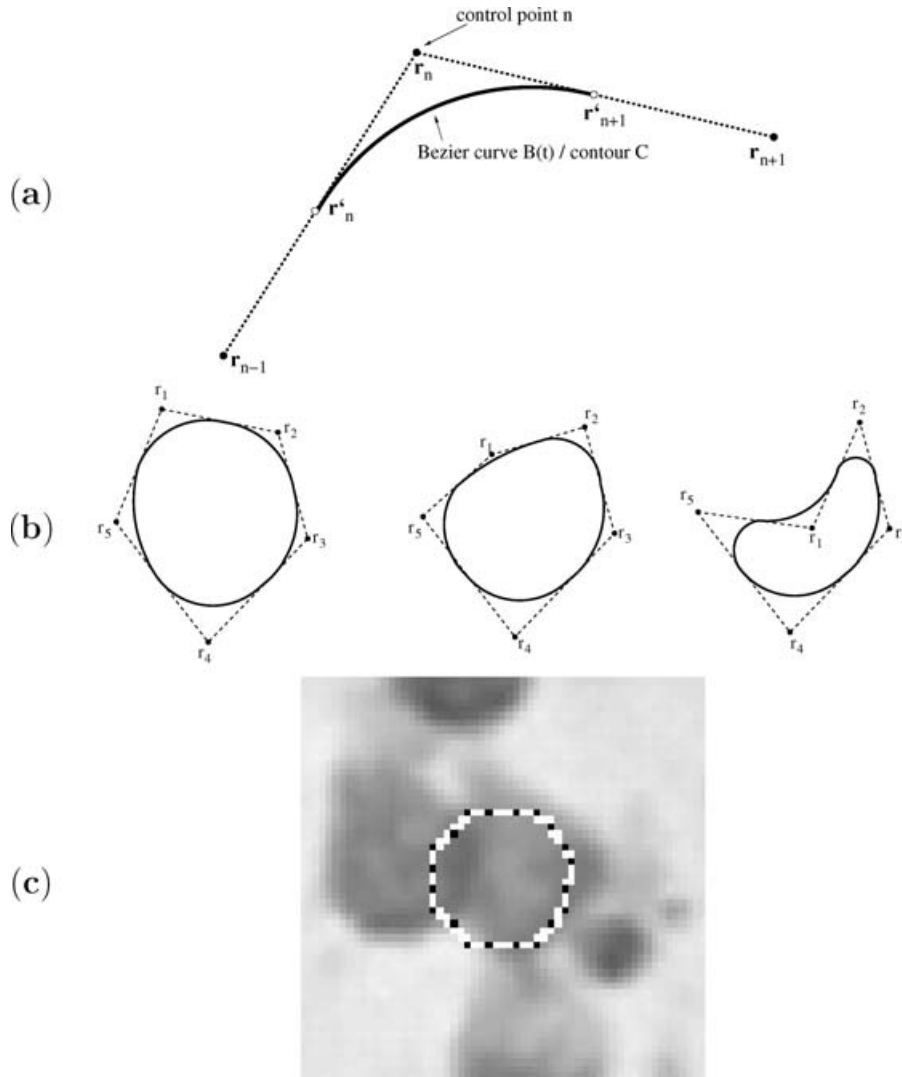


**Fig. 5.** (a) The contour  $C$  is described by the control points  $r_1, r_2, \dots, r_N$ . (a) Quadratic Bezier curve  $B(t)$  is defined for control point  $n$  using the control points  $r_{n-1}, r_n$ , and  $r_{n+1}$ . The points  $r'_n$  are halfway between  $r_{n-1}$  and  $r_n$ . The equation for the contour is  $B(t) = (1-t)^2 r'_n + 2t(1-t)r_n + r'_{n+1}t^2, t = 0..1$ . The equations guarantee that at the points  $r'$  the curve is continuous and smooth. Combining several Quadratic Bezier curves creates a quadratic B-spline contour. An example with 5 control points is presented in (b) which shows how the B-spline contour moves when one control point ( $r_1$ ) moves. (c) Contour  $C$  (white pixels) with 20 control points (single black pixels) that is overlaying the image.

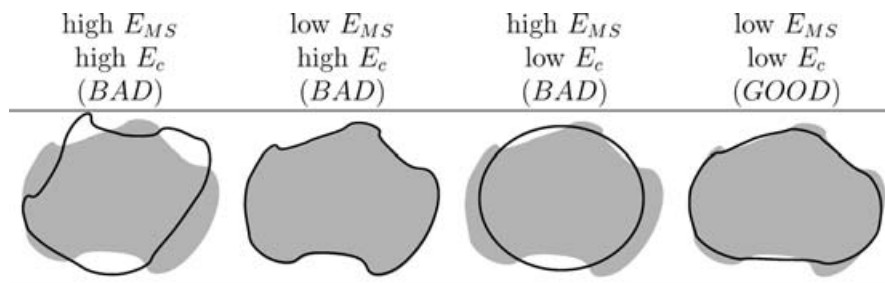


**Fig. 6.** Schematic drawing showing the relative energies of  $E_{MS}$  and  $E_c$  for the same image (shown as grey) and four different contour shapes (shown as black loops). The first three cases are examples of improperly fit contours with a high overall energy  $E = E_{MS} + \alpha E_c$ . The last case is an example of an optimal contour minimizing the overall energy.

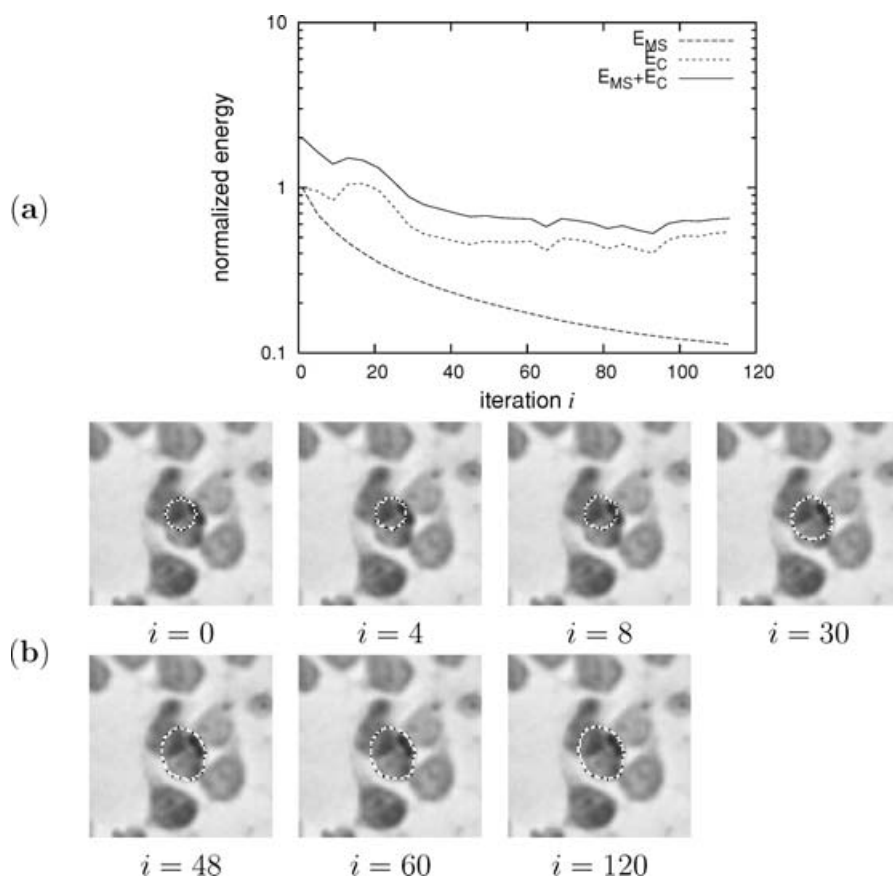


**Fig. 7.** Examples of the active contour movement within the image during the OSM segmentation phase. The number of control points (black dots) is 20. The B-spline contour is white. The contour starts at a location determined by the overmarking step of the OSM. (a) Evolution of the energy terms  $E_{MS}$  and  $E_c$ . (b) Contour evolution after 0, 4, 8, 30, 48, 60, and 120 steps. When a local minimum is reached, the contour no longer moves, and the points internal to the contour are saved.

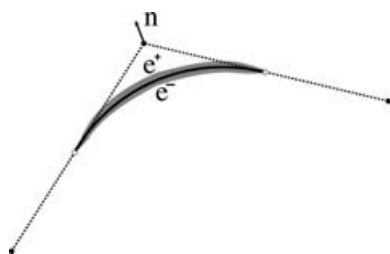


**Fig. 8.** Control point movement based on  $E_{MS}$  follows Eq. (12). The terms  $e^+$  and  $e^-$  are  $E_{MS}$  (Eq. 3) integrated over the single line of pixels right outside ( $e^+$ ) and right inside ( $e^-$ ) of the contour centred around each control point  $n$ .  $\mathbf{n}_x$  and  $\mathbf{n}_y$  are the  $x$  and  $y$  components of the outer normal vector of  $C$  at the control point.

Here  $\langle \rangle$  denotes the sample average.  $z_0$  is a  $2N$  vector and  $\Sigma$  is a  $2N \times 2N$  matrix. Creating  $z_0$  and  $\Sigma$  for a set of shapes  $\chi = \{z_1, z_2, \dots\}$  is equivalent to modeling the distribution of shapes in  $\mathbb{R}^{2N}$  as a Gaussian distribution (Cremers *et al.*, 2000).

To minimize  $E_c(C)$ , the following evolution equation for each control point is used:

$$\dot{z}(t) = \Sigma^{-1} (z(t) - z_0). \quad (11)$$

Combining the two Eqs (5) and (11) gives the final evolution equations for each control point  $n$  during each iteration:

$$\begin{aligned} x_n(t + dt) &= x_n(t) + \left\{ (e^+ - e^-) \mathbf{n}_x \right. \\ &\quad \left. + \alpha [\Sigma^{-1} (z(t) - z_0)]_{2n-1} \right\} dt \\ y_n(t + dt) &= y_n(t) + \left\{ (e^+ - e^-) \mathbf{n}_y \right. \\ &\quad \left. + \alpha [\Sigma^{-1} (z(t) - z_0)]_{2n} \right\} dt, \end{aligned} \quad (12)$$

recalling that  $e^+$  and  $e^-$  are  $E_{MS}$  (Eq. 3) summed over the single line of pixels right outside ( $e^+$ ) and right inside ( $e^-$ ) the segment of  $C$  centred around control point  $(x_n, y_n)$  (Fig. 8), and are dependent on  $\lambda$  and  $u_{ij}$ .

The evolution of the contour is driven by Eqs (6, 12), with variables  $u_{ij}$  and contour points  $(x_1, y_1, \dots, x_N, y_N)$ . Note that Eqs. (6, 12) are coupled and must be solved simultaneously.

Performing a step by step evolution of the control points (Eq. 12) and  $u_{ij}$  (Eq. 6),  $C$  evolves in the following way: If  $C$  begins to change into a contorted, non-ovular shape to minimize  $E_{MS}$  (such as ‘leaking’ out of an area of weak or missing boundary information in the image), then  $E_c$  will increase, hence there will be a force opposing the movement. Similarly, if the contour begins to move back to a perfect oval to minimize  $E_c$ ,  $E_{MS}$  will increase and thus limit such a change. When a local minimum is reached and the contour no longer moves, the points internal to the contour are saved, and the process starts again at a new location until all starting locations are exhausted.

There are several free parameters ( $\alpha$ ,  $\lambda$ ,  $dt$ ,  $N$ , etc.) that must be set within the OSM algorithm. Some of these parameters, called *secondary parameters*, do not greatly affect the evolution, and can be set the same for all Nissl-stained images. The secondary parameters are as follows:  $N$  is set to 20, so that for a typical 80  $\mu\text{m}$  circumference of a neuron cell body, neighbouring control points are 3  $\mu\text{m}$ , or roughly 4 pixels away from each other.  $z_0$  and  $\Sigma$  define the training that depend on the typical shapes of the object of interest, in our case a neuron. We build these parameters by creating a sample of 100 ellipses, ranging linearly from an eccentricity of 0–0.4, a simple representation of the average shape of neuron cell bodies. To speed up the evolution, we allow for different ‘time’ steps and Mumford–Shah parameters in Eqs (12.6). In Eq. (12),  $dt \rightarrow dt_c$  and  $\lambda \rightarrow \lambda_c$ . In Eq. (6),  $dt \rightarrow dt_u$  and  $\lambda \rightarrow \lambda_u$ . In this schema,  $dt_c$ ,  $dt_u$  and  $\lambda_u$  can be set as secondary parameters which do not need to change for any of the pictures. We set  $dt_c = 100$ ,  $dt_u = 0.05$  and  $\lambda_u = 1$ .

In addition to the secondary parameters, there are two *primary parameters* which greatly affect segmentation, and must be determined empirically: the energy ratio  $\alpha$  between  $E_{MS}$  and  $E_c$ , and the energy parameter  $\lambda_c$  within the  $E_{MS}$  term.

Because the active contour algorithm described above was designed for generic object recognition, the algorithm itself (in addition to the free parameters) can be ‘tuned’ for the task of finding dark elliptical features that are overlapping or relatively close to each other on a lighter background. We adjust the above algorithm in a simple way to accommodate overlapping: if  $f_{ij} - u_{ij}(t) > 0$  near and inside the given control point, the contour is ‘leaking’ out to find the edge of another feature next to it. We therefore multiply this control point’s contribution to  $E_{MS}$  by a free parameter  $\eta$  greater than 1. Here,  $\eta$  is a secondary parameter, and is set to 1.5 for all images.

We now discuss each step in ANRA.

#### Step I: Image acquisition

We test ANRA on Nissl-stained tissue samples of seven young adult (6.4–11.8 years; mean 8.5 years) and seven aged (24.7–32.9 years; mean 30.1 years) female Rhesus monkey subjects that were part of an ongoing study of the effects of aging on cognitive function (Cruz *et al.*, 2004). For each subject, eight

(four from each of two sections) grey scale (1–256)  $512 \times 512$  pixel images with 1.5 pixels  $\mu\text{m}^{-1}$  resolution ( $\sim 150$  neurons per image) were taken from area 46, layer III of the prefrontal cortex in the ventral bank of sulcus principalis. Three subjects had appreciable differences in image quality between the two sections, therefore the total number of different subject/image-quality is 17. Figure 2(b) shows 12 of the 17 subject/image-quality.

#### Step II: Segmentation training

All images are normalized as described in Section ‘Image input and preprocessing’. Out of each of the 17 subject/image-quality, one image is randomly selected as a *training image*. The digital image is marked for neuron cell bodies by an expert observer who ‘paints’ sets of pixels over the neurons using a small graphical program. Different objects can share pixels, or overlap, but the sets exist as separate entities even if there is an overlap. We designate these sets of pixels created by an expert observer the *training segments*. The training segments will be compared to *computer segments* from the OSM output. The manual identification is relatively quick (2–4 seconds per neuron), and does not require a model image, i.e.: no feature overlap (Lin *et al.*, 2005). Furthermore, the cell marking method creates knowledge of the extents of each cell body as viewed by an expert observer, independent of and unbiased to our segmentation procedure. This information is saved and used repeatedly for multiple training runs as needed, and does not have to be repeated for the same image if different training parameters are checked (de Solórzano *et al.*, 1999; Lin *et al.*, 2005).

We next determine the values of the primary parameters  $\alpha$  and  $\lambda_c$ , the two primary free parameters which greatly affect the segmentation. We find that there is significant loss in functionality when  $\alpha$  is outside the  $[10^{-9}, 10^{-8}]$  range and  $\lambda_c$  is outside the  $[1, 5]$  range. We therefore search this space of  $\alpha$  and  $\lambda_c$  by comparing the resulting computer segments to the training segments. A training segment is ‘found’ if the computer segment shares more than 70% of the pixels with the training segment (Fig. 9). The set called the final OSM parameters, denoted  $\alpha^*$  and  $\lambda_c^*$ , is the set that correctly identifies 95% or more training segments. The  $(\alpha^*, \lambda_c^*)$  values are then recorded and used for the rest of ANRA.

The OSM with the correct primary parameters ( $\alpha^*$ ,  $\lambda_c^*$ ) identifies 95% or more of neurons in the images, but it also identifies other non-neuron objects, such as staining errors, glial cells, and improper coverings of neurons. To separate neurons from non-neurons, computer training is performed.

First, we compare the  $(\alpha^*, \lambda_c^*)$ -parameter OSM computer segments to the training segments. Each computer segment is either placed in the neuron segment category or non-neuron segment category based on whether the segment mutually overlaps any training segment (Fig. 9). Second, each segment is represented by seven *segment properties*  $\mathbf{v} = (v_1, v_2, \dots,$

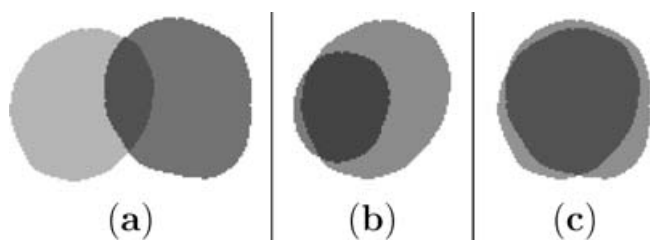


**Fig. 9.** Two segments represent the same object when they *mutually* share more than 70% of their pixels. The two segments in (a) do not pass the required criteria because neither segment overlaps the other by more than 70%. The two segments in (b) do not pass the required criteria because only one segment overlaps the other by more than 70%. Only in (c) does the required overlap occur. This analysis is used when computer segments are compared to ‘gold standard’ training segments and either designated a neuron or non-neuron, and during the overlap deletion phase, when the segment with the highest probability of being a neuron is selected among all overlapped segments.

$v_7$ ). The seven segment properties are chosen to be the most salient measures of identifying neurons within an image. For the calculations of the segment properties, we denote the total number of pixels within the segment as  $A_c$  and the total number of pixels within the contour as  $|C|$ . The properties are based on the optical density of the original image  $f_{ij}$  as well as the square of the magnitude of the image gradient  $|\nabla f_{ij}|^2$ . The segment properties are presented in Table 1.  $\sum^A$  is a sum over all of the pixels within the segment area,  $\sum^C$  is a sum over the edge pixels of the segment circumference,  $r_c$  is the location of the centre of the segment, and  $r_{ij}$  is the location of the pixel ( $ij$ ).

Using the WEKA machine learning toolkit (Witten & Frank, 2005), we assess the following machine learning algorithm’s ability to discriminate between neuron property vectors  $\{v_1^+, v_2^+, \dots\}$  and non-neuron property vectors  $\{v_1^-, v_2^-, \dots\}$ : the 1-rule classifier (Holte, 1993), naive Bayes classifier (John & Langley, 1995), support vector machine classifier (Platt, 1998), nearest neighbour classifier (Aha & Kibler, 1991), decision tree classifiers (Quinlan, 1993), Bayes net and multilayer perceptron (Witten & Frank, 2005). The cost between Type 1 errors (marking a non-neuron property vector as a

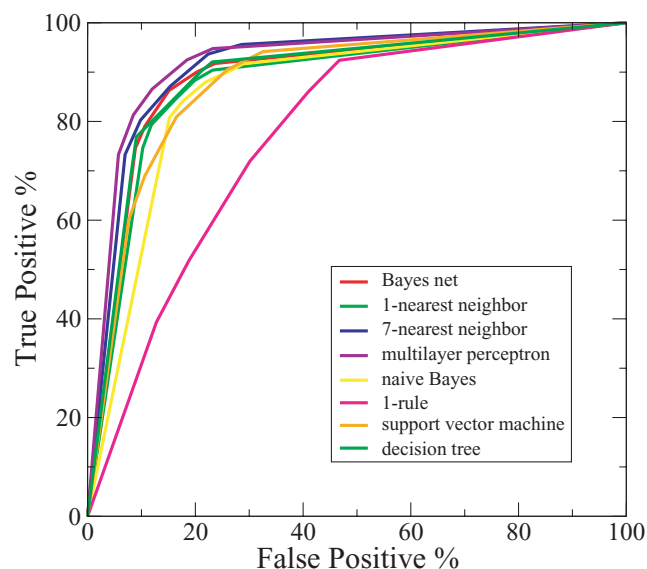


**Fig. 10.** Receiver operating characteristic (ROC) curve for each training method evaluated. It is seen that the Multilayer Perceptron (MLP) has the best ROC curve – the highest percentage of neuron property vectors identified with the smallest percentage of non-neuron property vectors incorrectly identified. MLP is chosen as the main training method for ANRA.

neuron) and Type 2 errors (marking a neuron property vector as a non-neuron) is scanned by tuning the cost ratio term in the training algorithm. A stratified cross-validation evaluation for various cost ratios (3:1, 2:1,  $\dots$ , 1:10) creates a receiver operator characteristic (ROC) curve (Duda *et al.*, 2001) for each training method (Fig. 10). The Multilayer Perceptron (MLP) using a single, 4-node hidden layer, has the best ROC curve, as it provides the highest percentage of neuron property vectors identified and the smallest percentage of non-neuron property vectors incorrectly identified. MLP is therefore chosen as the main training method for ANRA.

### Step III: Application

Automatic neuron recognition is now applied on an unlimited number of other images that are normalized and similar in

**Table 1.** Segment properties used in training.

	Description	Equation
$v_1$	Segment area	$A_c$
$v_2$	Average optical density ( $\bar{f}$ )	$\frac{1}{A_c} \sum^A f_{ij}$
$v_3$	Variance of optical density	$\frac{1}{A_c} \sum^A (f_{ij} - \bar{f})^2$
$v_4$	Radius of gyration of optical density	$\frac{1}{A_c} \sum^A  r_{ij} - r_c  f_{ij}$
$v_5$	Segment edge length ( $ C $ ) versus segment area	$ C /A_c$
$v_6$	Average gradient of segment edge	$\frac{1}{ C } \sum^C  \nabla f_{ij} ^2$
$v_7$	Average change in gradient of segment edge	$\frac{1}{ C } \sum^C  \nabla f_{i+1j} ^2 -  \nabla f_{ij} ^2$

morphology to the training images. The steps are as follows:

1. The OSM with the primary parameters ( $\alpha^*$ ,  $\lambda_c^*$ ) is performed on the new image.
2. The properties  $v$  are calculated for each computer segment.
3. A cost ratio is selected by the user.
4. All computer segments deemed non-neurons by the MLP are discarded.
5. For any two remaining computer segments that mutually overlap by more than 70%, the computer segments with the smaller probability of being a neuron (as determined by the MLP) is discarded.

The  $(x, y)$  centres, sizes, and shapes of the remaining computer segments are the final result of ANRA.

#### Comparison method

A semi-automatic method (semi-auto) was used in prior neuron density maps correlation studies (Cruz *et al.*, 2005). In the semi-auto method a combination of computer software and human intervention for each image is employed to identify neurons. Because the amount of human intervention scales with the number of images analyzed, the semi-auto method represents a standard with which we evaluate our completely automated recognition method.

#### Density map method and microcolumnar strength

We give a description of the density map method, as it is the main analysis to be applied to the results of ANRA. The density map method was initially described by Buldyrev *et al.* (2000) and a more detailed description and validation was given by Cruz *et al.* (2005). The density map is a 2D representation of the density correlation function  $g(x, y)$ , which uses as input the  $(x, y)$  locations of all neurons in the region of interest (ROI). This function  $g(x, y)$  is mapped to a two-dimensional grey scale image (density map) in which different shades of grey are proportional to the average local neuronal density. Thus, the density map quantifies the average neuronal neighbourhood surrounding a typical neuron within the ROI.

Operationally, the density map is calculated by first assigning indices ( $i = 1, 2, 3, \dots, N$ ) to all the neurons in the sample. Next, we centre a grid of bins of size  $D$  over each neuron and count how many other neurons fall in each bin constructing one matrix of accumulated neurons  $m(x, y)$ . We define  $g(x, y) = m(x, y)/N \cdot D \cdot 2$ , in which  $g(x, y)$  has units of an average density of objects at position  $(x, y)$ . As an example, the density map would be uniform if locations of objects (neurons) are uncorrelated, but will show patterns when there are regular spatial arrangements between the objects.

For the case of neurons forming microcolumns, their density map exhibits one central vertical ridge, sometimes accompanied by two less pronounced parallel neighbouring ridges. For this study, we are interested in the microcolumn strength  $S$ , which is extracted from the density map by

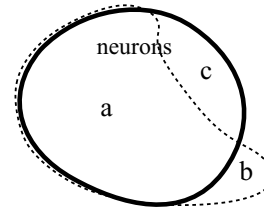


**Fig. 11.** Venn diagram showing the relative quantities for evaluating the quality of a neural recognition method. The bold black line separates neuron from non-neuron objects in the image. The dotted area shows the objects that are identified by a method. The method correctly identifies most of the neurons (a), but misses some neurons (c) and identifies some non-neurons as neurons (b). Using the quantities a, b and c, standardized percentages of neuron versus non-neurons can be calculated.

taking the ratio of the neuronal density within the average microcolumn to the average neuronal density (Cruz *et al.*, 2005). For the same images,  $S$  is calculated using ANRA  $(x, y)$  locations as well as semi-automatic  $(x, y)$  locations, and the results are compared.

#### Results

For each of 17 subject/image-qualities, an *evaluation image* is randomly selected from the remaining images and marked for neuron cell bodies by the expert. The evaluation image is used as a 'gold standard' to assess the accuracy of ANRA and the comparison methods. A total of 2448 'gold standard' neurons are analyzed, for an average of 144 neurons per subject/image-quality. For each of the two recognition methods (semi-auto and ANRA), we compare the method's identified neurons to the 'gold standard', and retrieve the following numbers (Fig. 11):

$$a = \text{number of correctly identified neurons,} \quad (13)$$

$$b = \text{number of non-neurons incorrectly identified as neurons,} \quad (14)$$

and

$$c = \text{number of non-identified neurons.} \quad (15)$$

To compare methods for the different subject/image-qualities, we define the following normalized metrics:

$$A = \frac{a}{a + c} \times 100, \quad (16)$$

and

$$B = \frac{b}{a + c} \times 100. \quad (17)$$

$A$  is the percent of correctly identified neurons ('true positives').  $B$  is the percentage of non-neurons that are incorrectly identified as neurons ('false positives').

The results are shown in Fig. 12. The semi-auto method is characterized by one  $(A, B)$  set. Because of the ability to adapt

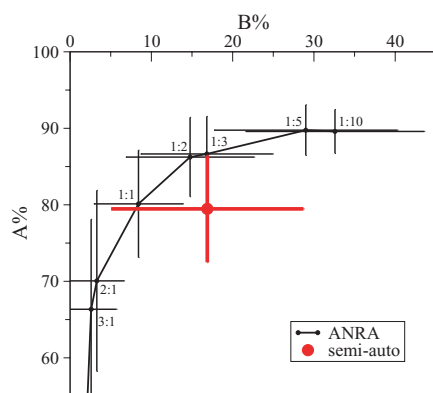


**Fig. 12.** Results of ANRA. The semi-auto method is characterized by one (A, B) set. Because of the ability to adapt the cost ratio as described in Section ‘Step III: Application’, ANRA is shown at 7 different ratios (3:1, 2:1, 1:1, 1:2, 1:3, 1:5 and 1:10), creating an ‘adapted’ ROC curve. Since each point is an average of the 17 subject/image-types, the error bars show the standard deviation of the spread for both A and B.

**Table 2.** Results of ANRA for 1:2 cost ratio.

#	Semi-auto		ANRA	
	A(%)	B(%)	A(%)	B(%)
1	81	13	82	11
2	71	14	84	7
3	82	14	91	21
4	79	15	78	4
5	90	43	92	30
6	65	3	85	16
7	76	18	87	21
8	83	15	88	6
9	76	12	93	15
10	79	10	85	23
11	73	6	77	7
12	82	4	88	11
13	92	44	84	6
14	90	26	95	16
15	80	20	80	11
16	77	23	91	28
17	75	7	86	17
Avg.	80 ± 7	17 ± 12	86 ± 5*	15 ± 8

the cost ratio as described in Section ‘Step III: Application’, ANRA is shown at seven different ratios (3:1, 2:1, 1:1, 1:2, 1:3, 1:5 and 1:10), ranging from very selective, to no selectivity, creating an ‘adapted’ ROC curve. Since each point is an average of the 17 subject/image-quality, the error bars show the standard deviation of the spread for both A and B. We choose the 1:2 cost ratio for further analysis because it is at the inflection point of the ‘adapted’ ROC curve (Fig. 12), and it has the closest average (A,B) to that of semi-auto. Table 2 and Fig. 13(a) shows the individual results for each subject/image-quality for the semi-auto method and the ANRA with 1:2 cost

ratio. Figure 13(b) shows an example of semi-auto and ANRA points compared to the gold standard.

The results show that ANRA has a significantly higher A value of recognition ( $P$ -value: 0.002) and a similar B value of recognition compared to the semi-auto method.

We also compare microcolumnar strength  $S$  (Section ‘Density map method and microcolumnar strength’) using the  $(x, y)$  locations from both ANRA and semi-auto methods of neuron identification for the entire image database of rhesus monkey subjects as described in Section ‘Step II: Segmentation training’. Fourteen thousand neuron locations were used, for an average of 1000 neuron locations for each subject. We find significant correlations between microcolumnar strength measurements of the ANRA and semi-auto methods of neuron recognition (Fig. 14). This shows that ANRA has the ability to find significant changes in advanced neuron spatial arrangements within different subjects, and can therefore be applied to large data sets where manual or semi-auto recognition are not viable.

## Discussion

In this work, we introduce a method called an ANRA which uses a combination of image segmentation and machine learning to retrieve neuron locations within digitized images of Nissl-stained Rhesus monkey brain tissue. Despite challenges, such as overlapping of neuron cell bodies and the presence of glial cells and artefacts in the tissue, we demonstrate that ANRA has a significantly better recognition capability than a semi-auto method (Cruz *et al.*, 2005) which requires expert manual intervention for each image. ANRA’s recognition quality is combined with computational efficiency, resulting in recognition of  $\sim 100$  neurons per minute using a standard personal computer. Consequently, large numbers of neuron locations can be retrieved, spanning considerably larger brain regions than ever before. Furthermore, because ANRA is capable of efficiently extracting neuron locations from durable and commonly used Nissl-stained tissue, it can potentially be applied to vast stores of archival material existing in laboratories and research collections around the world.

Such a large data set of  $(x, y)$  neuron locations will allow for a variety of systematic analyses that have previously not been possible. The ability to identify every neuron in entire sections of the brain will allow for both global and local analyses of neuron numbers, glial cell numbers, regional cell densities, and local variations in cell densities. Also, as was shown in the ‘Results’ section, studies of microcolumnarity or other spatial features of cortex, including spatial inter-relationships among neurons and glia using autocorrelation and cross-correlation, are possible. Lastly, ANRA also allows for less obvious applications, including the investigation of the spatial network of the brain using the neuron locations as nodes. None of these studies are possible with the elegant sampling methods of modern stereology.

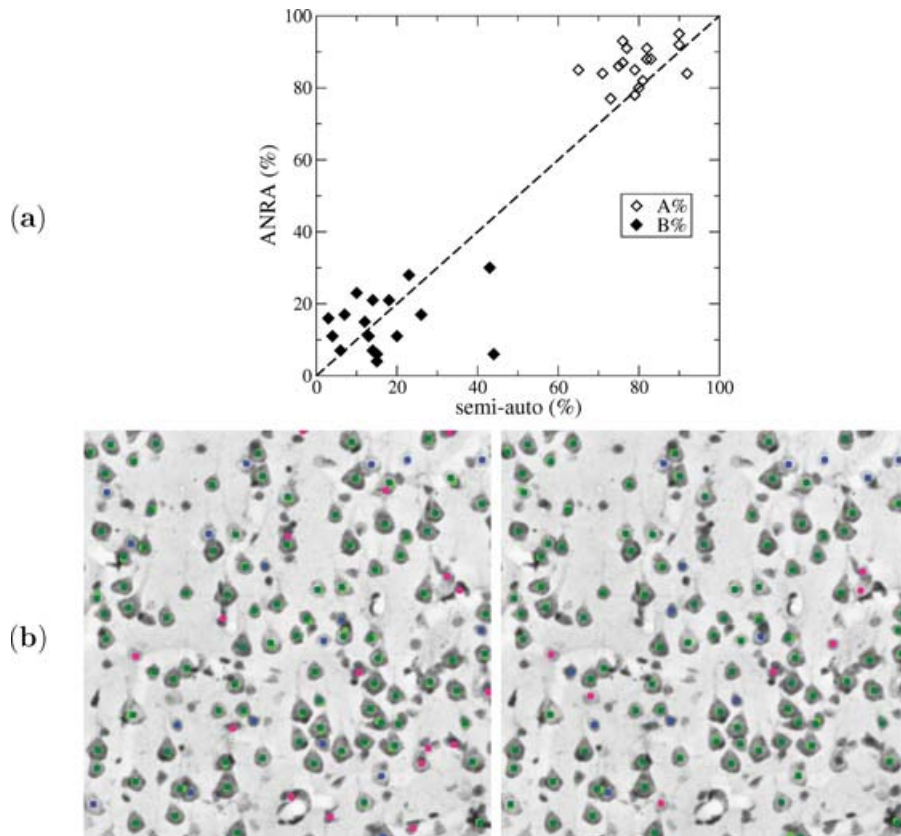


**Fig. 13.** (a) Individual results for 17 subject/image-types for the semi-auto method and the ANRA (with 1:2 cost ratio). (b) Recognition results for the semi-auto method (left) and the ANRA method (right) for example subject/image-quality #1 (Table 2). Dark green: gold standard marks that match with the method. Blue: gold standard marks that DO NOT match with the method. Light Green: method points that match with gold standard points. Pink: method points that do not match with gold standard points.

We highlight the need for large data sets of neuron locations ( $10^3$ – $10^4$ ) in comparative studies proposed in the Introduction and defined in Section ‘Density map method and microcolumnar strength’. Generally, the goal of a comparative study is to find a statistically significant difference in a measured quantity (i.e. microcolumn strength) due to a change in an independent variable (age, species, sex, disease state, etc.). In the case of a 1D correlation between nearest neighbours or the 2D microcolumnar analysis, the neuron locations are used to create 1D and 2D histograms, respectively. The number of neurons must be high enough to resolve the effect of the independent variable above random noise of the histogram. Buldyrev *et al.* (2000) showed that for a resolution of interest (seeing 3% changes between 10  $\mu\text{m}$  bins),  $\sim 10^4$  neuron locations are needed in the comparative study of microcolumnarity. For the same resolution in a 1D correlation comparative study, such as nearest-neighbour distances, only  $\sim 1000$  neurons are needed (Schmitz *et al.*, 2002). For a given bin size, the theoretical calculation shows that the required number of neurons scales as a power of dimensions that are being correlated. Thus, automatic recognition becomes critical in higher dimension correlations. As an example we consider

a 30 subject study of neuron spatial arrangement using  $\sim 10^5$  neuron locations, making 100 different measurements of 1000 neurons each through a certain layer across several Brodmann regions. The semi-automatic approach, which allows for acquisition of 10 neurons per second, would take 83 human hours to complete. Comparatively, ANRA could complete the same task in 24 h on 20 Intel P4 processors with less than 1 h of preparation time.

ANRA has a further advantage of reducing experimental drift. Specifically, in terms of human bias, the ‘criteria’ for neuronal identification will necessarily differ between different observers that are often required for a huge analysis extending over months to years, whereas ANRA’s criteria, once established from the training algorithm, remains constant. Furthermore, ANRA’s criteria will not be subject to the kind of experimental drift that can occur over time when one observer manually identifies thousands of neurons over a period of weeks to months.

Recently, there have been advances in level set methods to recognize overlapped cell nuclei (de Solórzano *et al.*, 1999; Lin *et al.*, 2007). The recognition challenges with Nissl-stained tissue are far greater than the challenges of confocal

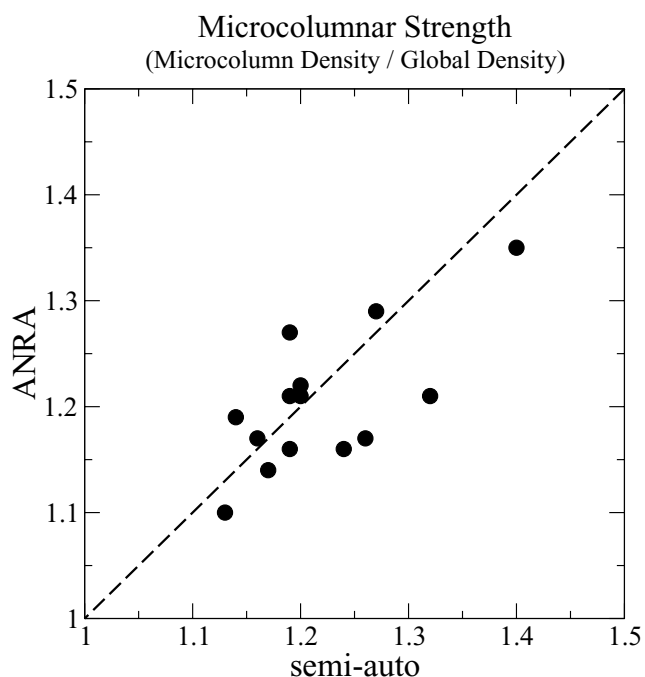


**Fig. 14.** Comparison of microcolumnar strength measurement ( $S$ ) using the  $(x, y)$  locations from both ANRA (with 1:2 cost ratio) and semi-auto methods of neuron identification. A total of 14,000 neuron locations were used, for an average of 1000 neuron locations for each subject (plot point). Both the neuron density and microcolumnar strength show significant correlations of ANRA with the semi-auto method.

microscopy using fluorescence. Lin *et al.* (2007) show how neurons and glial cells completely separate into two regions of parameter space using only two parameters (texture and intensity) of the identified segmentations. If plotted in a similar way, no two parameters that we consider (size, intensity, texture, gyration, edge versus area, etc.) would yield such a separation. Thus, in a Nissl-stained tissue visualized by optical microscopy, the parametrized method of Cremers *et al.* (2000), which, by design, overcomes the challenges of noisy images and missing boundary data (Section 'Active contour segmentation'), is most efficient.

Our results suggest that the ANRA method is performing at maximal efficiency: when a second expert's marks are compared with the gold standard on the same Nissl-stained image, the performance ( $A = 88 \pm 5\%$ ) is not significantly higher than ANRA's performance ( $A = 86 \pm 5\%$ ).

Although there are 10 free parameters within the algorithm, only two of them called the *primary parameters* must be explored to find the correct values for proper segmentation. These *primary parameters* are automatically found in the OSM parameter search during training. The other eight free parameters, which we call the *secondary parameters*, can be fixed for the general task of identifying elliptical features within noisy images with missing boundary data, thereby solidifying them for the broadly applicable problem of neuron recognition

in all Nissl-stained tissue. For a given morphological feature of interest, once a small set of representative images have been trained to, the training and parameters can be reused, due to the normalization of images of different quality. This setup will allow for the study of large areas of montaged images, or large data sets of hundreds of slides, all with the same training. Furthermore, the free parameters and training can be adapted for identification of other types of neurons, glial cells, etc.

Lastly, because of the modular nature of the method (Fig. 1), it will be relatively easy to replace partial aspects of the overall algorithm by considering advances in recent published work. For example, Tscherepanow *et al.* (2006) independently developed a method to identify living cells that uses a larger set of training properties that is reduced with principle/independent component analysis, and Costa & Boltt (2006) has applied advanced pattern matching to the identification of neuron cell bodies in Nissl-stained tissue. By replacing the respective aspects of ANRA with such methods, the ideal overall identification algorithm can be found for not only the recognition of neuron cell bodies, but also the recognition of other objects of scientific interest, for example living cells or glial cells.

#### Acknowledgements

This work was supported by the National Institutes of Health grants R01-AG021133, P01-AG00001 and P51-RR00165, the Alzheimer Association, and the Bechtel Foundation.

#### References

- Aha, D. & Kibler, D. (1991) Instance-based learning algorithms. *Mach. Learn.* **6**, 37–66.
- Asare, E. (1996) Neuronal pattern correlates with the severity of human immunodeficiency virus-associated dementia complex. *Am. J. Pathol.* **148**, 31–36.
- Benali, A., Leefken, I., Eysel, U. F. & Weiler, E. (2003) A computerized image analysis system for quantitative analysis of cells in histological brain sections. *J. Neurosci. Meth.* **125**, 33–43.
- Blake, A. & Isard, M. (1998) *Active Contours*. Springer, London.
- Buldyrev, S. V., Cruz, L., Gomez-Isla, T., Gomez-Tortosa, E., Havlin, S., Le, R., Stanley, H. E., Urbanc, B. & Hyman, B. T. (2000) Description of microcolumnar ensembles in association cortex and their disruption in alzheimer and lewy body dementias. *Proc. Natl. Acad. Sci.* **97**, 5039–5043.
- Buxhoeveden, D. & Lefkowitz, W. (1996) The linear organization of cell columns in human and non-human anthropoid tpt cortex. *Anat. Embryol.* **194**, 23–36.
- Casanova, M. F., Switala, A. E. & Trippe, J. (2006) A comparison study of the vertical bias of pyramidal cells in the hippocampus and neocortex. *Dev. Neurosci.* **29**, 193–200.
- Costa, L. & Boltt, E. (2006) A fast and accurate nonlinear spectral method for image recognition and registration. *Appl. Phys. Lett.* **89**, 174102.
- Cremers, D., Schnorr, C., Weikert, J. & Shelleward, C. (2000) Diffusion-snakes using statistical shape knowledge. In *Algebraic Frames for the*

- Perception-Action Cycle, Lecture Notes in Computer Science* (ed. by G. Sommer & Y.Y. Zeevi), Vol. 1888, pp. 164–174. Springer, Heidelberg, Germany.
- Cruz, L., Buldyrev, S., Peng, S., Roe, D., Urbanc, B. & Stanley, H. (2005) A statistically based density map method for identification and quantification of regional differences in microcolumnarity in the monkey brain. *J. Neurosci. Meth.* **141**, 321–332.
- Cruz, L., Roe, D. L., Urbanc, B., Cabral, H., Stanley, H. E. & Rosene, D. L. (2004) Age-related reduction in microcolumnar structure in area 46 of the rhesus monkey correlates with behavioral decline. *Proc. Natl. Acad. Sci.* **101**, 15846–15851.
- de Solórzano, C. O., Rodriguez, E. G. A., Jones, A., Pinkel, D., Gray, J. W., Sudar, D. & Lockett, S. J. (1999) Segmentation of confocal microscope images of cell nuclei in thick tissue sections. *J. Microsc.* **193**, 212–226.
- Duda, R., Hart, R. & Stork, D. (2001) *Pattern Classification*. John Wiley and Sons, New York, USA.
- Duyckaerts, C. & Godefroy, G. (2000) Voronoi tessellation to study the numerical density and the spatial distribution of neurons. *J. Chem. Neuroanat.* **20**, 83–92.
- Hof, P. R., Haroutunian, V., Friedrich, V. L., Jr., Byne, W., Buitron, C., Perl, D. P., & Davis, K. L. (2003) Loss and altered spatial distribution of oligodendrocytes in the superior frontal gyrus in schizophrenia. *Biol. Psychiat.* **53**, 1075–1085.
- Holte, R. (1993) Very simple classification rules perform well on most commonly used datasets. *Mach. Learn.* **11**, 63–91.
- Javi, B. (2002) *Image Recognition and Classification: Algorithms, Systems, and Applications*. Marcel Dekker, New York, USA.
- John, G. H. & Langley, P. (1995) Estimating continuous distributions in bayesian classifiers. In *Proceedings of the Eleventh Conference on Uncertainty in Artificial Intelligence* 338–345.
- Krasnoperov, R. A. & Stoyan, D. (2004) Second-order stereology of spatial fibre systems. *J. Microsc.* **216**, 156–164.
- Lin, G., Chawla, M. K., Olson, K., Barnes, C. A., Guzowski, J. E., Bjornsson, C., Shain, W. & Roysam, B. (2007) A multi-model approach to simultaneous segmentation and classification of heterogeneous populations of cell nuclei in 3D confocal microscope images. *Cytom. Part A* **71A**, 724–736.
- Lin, G., Chawla, M. K., Olson, K., Guzowski, J., Barnes, C. & Roysam, B. (2005) Hierarchical, model-based merging of multiple fragments for improved three-dimensional segmentation of nuclei. *Cytometry* **63A**, 20–33.
- Long, X., Cleveland, W. L. & Yao, Y. L. (2005) A new preprocessing approach for cell recognition. *IEEE T. Inf. Technol.* **5**, 407–412.
- Long, X., Cleveland, W. L. & Yao, Y. L. (2006) Automatic detection of unstained viable cells in bright field images using a support vector machine with an improved training procedure. *Comput. Biol. Med.* **36**, 339–362.
- Mayhew, T. M. (1991) A review of recent advances in stereology for quantifying neural structure. *J. Neurocytol.* **21**, 313–328.
- Mumford, D. & Shah, J. (1989) Optimal approximation by piecewise smooth functions and associated variational problems. *Commun. Pur. Appl. Math.* **42**, 577–685.
- Nattkemper, T. W., Ritter, H. J. & Schubert, W. (2001) A neural classifier enabling high-throughput topological analysis of lymphocytes in tissue sections. *IEEE T. Inf. Technol.* **5**, 138–149.
- Peng, S., Urbanc, B., Cruz, L., Hyman, B. T. & Stanley, H. E. (2003) Neuron recognition by parallel potts segmentation. *Proc. Natl. Acad. Sci.* **100**, 3847–3852.
- Peters, M., Jancke, L., Staiger, J. F., Schlaug, G., Huang, Y. & Steinmetz, H. (1998) Unsolved problems in comparing brain sizes in homo sapiens. *Brain Cognition* **37**, 254–285.
- Platt, J. (1998) Fast training of support vector machines using sequential minimal optimization. In *Advances in Kernel Methods – Support Vector Learning* (ed. by B. Schoelkopf, C. Burges & A. Smola). MIT Press, Cambridge, MA, USA.
- Quinlan, R. (1993) *C4.5: Programs for Machine Learning*. Morgan Kaufmann Publishers, San Mateo, CA.
- Ray, N., Acton, S. T. & Ley, K. (2002) Tracking leukocytes in vivo with shape and size constrained active contours. *IEEE T. Med. Imaging* **21**, 1222–1234.
- Schmitz, C., Grolmes, N., Hof, P. R., Boehringer, R., Glaser, J. & Korr, H. (2002) Altered spatial arrangement of layer V pyramidal cells in the mouse brain following prenatal low-dose x-irradiation. a stereological study using a novel three-dimensional analysis method to estimate the nearest neighbor distance distributions of cells in thick sections. *Cereb. Cortex* **12**, 954–960.
- Schmitz, C. & Hof, P. R. (2005) Designed-based stereology in neuroscience. *Neuroscience* **130**, 813–831.
- Sjöström, P. J., Frydel, B. R. & Wahlberg, L. U. (1999) Artificial neural network-aided image analysis system for cell counting. *Cytometry* **36**, 18–26.
- Slater, D., Healey, G., Sheu, P., Cotman, C. W., Su, J., Wasserman, A. & Shankle, R. (1996) A machine vision system for the automated classification and counting of neurons in 3-D brain tissue samples. In *IEEE Workshop on Applications of Computer Vision (WACV)*. IEEE Computer Society, Washington, DC, USA.
- Todtenkopf, M. S., Vincent, S. L. & Benes, F. M. (2005) A cross-study meta-analysis and three-dimensional comparison of cell count in the anterior cingulate cortex of schizopphrenic and bipolar brain. *Schizophr. Res.* **73**, 79–89.
- Tscherepanow, M., Zöllner, F. & Kummert, F. (2006) Classification of segmented regions in brightfield microscope images. In *Proceedings of the 18th International Conference on Pattern Recognition*. IEEE Computer Society, Washington, DC, USA.
- Urbanc, B., Cruz, L., Le, R., Sanders, J., Hsiao-Ashe, K., Duff, K., Stanley, H., Irrizarry, M. C. & Hyman, B. T. (2002) Neurotoxic effects of thioflavin s-positive amyloid deposits in transgenic mice and alzheimers disease. *Proc. Natl. Acad. Sci.* **97**, 13990–13995.
- Witten, I. H. & Frank, E. (2005) *Data Mining: Practical Machine Learning Tools and Techniques*, 2 edition. Morgan Kaufmann, San Francisco
- Zimmer, C., Labruyère, E., Meas-Yedid, V., Guillén, N. & Olivio-Marin, J. (2002) Segmentation and tracking of migrating cells in videomicroscopy with parametric active contours: A tool for cell-based drug testing. *IEEE Trans. Med. Imaging* **21**, 1212–1221.